Materials Advances

ROYAL SOCIETY OF CHEMISTRY

PAPER

View Article Online
View Journal | View Issue

Cite this: *Mater. Adv.*, 2026, 7, 1704

First-principles investigation of $CuBiSeCl_2$: a quaternary halide chalcogenide material for advanced optoelectronic and thermoelectric energy harvesting and conversion technologies

Zihad Hossain,[a] Md. Riad Khan,[a] Sanzida Naznin Mim,[a] Md. Emon Hassan,[a] Mohammad Abdur Rashid[b] and Md. Lokman Ali *[a]

In response to the growing interest in multifunctional materials for energy conversion devices, $CuBiSeCl_2$ is systematically investigated as a quaternary halide chalcogenide with significant potential for both optoelectronic and thermoelectric applications. Utilizing density functional theory (DFT) and the semiclassical Boltzmann transport theory-based full-potential linearized augmented plane wave (FP-LAPW) technique, this study investigates the electronic, thermoelectric, optical and mechanical properties of $CuBiSeCl_2$. Structural optimization shows that the material crystallizes in an orthorhombic phase and the calculated elastic constants meet the Born stability criterion. Electronic calculations show that there is a direct band gap of about 0.737 eV at the high-symmetry Γ point. In contrast, anisotropy in the optical response shows that the crystal has a layered structure. The optical response also demonstrates strong absorption in the visible and UV range with a high refractive index, and a dielectric response, where the absorption spectrum is initiated near $\sim$0.8 eV and exceeds 1.5×10^5 cm^{-1} above 2 eV, highlighting its potential as an efficient light-harvesting material. Thermoelectric investigations indicate that $CuBiSeCl_2$ exhibits promising performance, where the Seebeck coefficient and electrical conductivity go up from 300 K to 600 K, which brings zT up to about 0.52. In contrast, zT reaches around 0.88 for temperatures ranging from 600 K to 900 K. However, calculated mechanical properties, such as bulk and shear moduli, show that $CuBiSeCl_2$is moderately stiff, while the Poisson ratio (0.304) and Pugh ratio (2.215) indicate its mechanical stability with moderate ductility. The average speed of sound is 2449.28 m s^{-1}, and the elastic Debye temperature is $\sim$257 K. Overall, these results show that $CuBiSeCl_2$ is a material with high potential for sustainable energy harvesting and conversion technologies.

Received 29th November 2025,
Accepted 10th December 2025

DOI: 10.1039/d5ma01386k

rsc.li/materials-advances

1. Introduction

Recently, the urgent search for renewable energy has become a global priority due to the depletion of fossil fuels and rising environmental concerns. In this context, the conversion of ambient waste heat and sunlight into electricity represents an eco-friendly and straightforward approach to addressing global energy challenges. Worldwide efforts are focused on developing high-performance thermoelectric (TE) and semiconductor materials for use in photovoltaic, optoelectronic, and thermoelectric technologies. With the advantages of green energy conversion, zero emissions, no mechanical parts, adaptability to varying temperatures, long service life, and compactness, TE generators have received significant attention.[1] Seebeck first discovered the thermoelectric effect in 1821, and it was later termed the Peltier effect when used to generate a temperature gradient *via* an electric current.[2] The performance of thermoelectric materials is commonly evaluated using the dimensionless figure of merit, $zT = S^2\sigma T/k = S^2\sigma T/(k_e/k_L)$, where T, σ, S, and $S^2\sigma$ are the absolute temperature, electrical conductivity, Seebeck coefficient, and power factor (PF), respectively. Also, k_e represents the thermal conductivity contributed by electrons and holes, while k_L denotes the thermal conductivity arising from phonons propagating through the crystal lattice.[3] Although increasing σ and S or reducing k can improve zT, the inherent interdependence among these parameters requires careful, synergistic adjustment.[4] Since lattice thermal conductivity is an intrinsic property, materials with naturally low values are ideal for enhancing the thermoelectric figure of

[a] *Department of Physics, Pabna University of Science and Technology, Pabna-6600, Bangladesh. E-mail: lokman.cu12@gmail.com*
[b] *Department Physics, Jashore University of Science and Technology, Jashore 7408, Bangladesh*

merit, zT. For a material to be considered an excellent thermoelectric (TE) candidate, its zT value should exceed unity.[5,6]

Numerous attempts have been made to enhance the thermoelectric figure of merit (zT) through innovative strategies. Multiple classes of materials, including inorganic and polymeric compounds, have been investigated for thermoelectric applications across diverse temperature ranges. Among them, inorganic semiconductors have proven to be the most effective,[7,8] with chalcogenide compounds receiving particular attention due to their promising properties. Building on this, recent research has turned toward mixed-anion systems, especially quaternary halide chalcogenides, which offer the dual advantages of intrinsically low thermal conductivity and favorable electronic characteristics.[9–11] Generally, quaternary halide chalcogenides are composed of four distinct elements: a monovalent cation (A), a p-block metal (M), a chalcogen (Ch, *e.g.*, S, Se, or Te), and a halogen (X, *e.g.*, Cl, Br, or I). This structural and compositional versatility of chalcogenides sets them apart from other material classes, enabling greater tunability of their physical properties through increased chemical and structural freedom.[12]

Recent experimental and theoretical research efforts have focused on improving the thermoelectric efficiency and increasing the zT of chalcogenide crystals. Several materials with intrinsically low thermal conductivity have been reported, including $Yb_{14}MnSb_{11}$ ($zT \approx 1.0$) by S. R Brown *et al.*,[13] single-crystal SnSe ($zT_{max} \approx 2.6$) by L. D. Zhao *et al.*,[14] and quaternary chalcogenides ($zT_{max} \approx 0.6$).[15–17] In a recent study, C. Wang *et al.*[18] reported a notable increase in zT for $Cu_{1-x}Ag_xInTe$, rising from 0.6 at $x = 0$ to 1.4 at $x = 0.25$. However, according to Wang *et al.*,[19] various copper-based chalcogenides like $Cu_{2-2x}Ag_xSe_{1-x}S_x$ exhibit high thermoelectric performance, with a sample of $Cu_{1.8}Ag_{0.2}Se_{0.9}S_{0.1}$ reaching a zT of 1.7 at temperatures exceeding 900 K.[20] Also, in a recent investigation,[21] the thermoelectric figure of merit (zT) for $AgSbTe_{2-x}Se_x$ reached 1.35 at 600 K at a doping level of $x = 0.02$. In 2022, Sujith *et al.*[22] employed first-principles calculations with spin–orbit coupling to investigate $CrSbSe_3$ and revealed optical anisotropy, suggesting its suitability for photovoltaic and optoelectronic applications.

To the best of our knowledge, the quaternary halide chalcogenide, $CuBiSeCl_2$, has received limited attention in the context of thermoelectric and optoelectronic applications. Motivated by this gap and the unique characteristics of the compound, we explore its thermoelectric and optoelectronic properties, and mechanical properties along with anisotropy using density functional theory (DFT) combined with semiclassical Boltzmann transport theory. The electronic structure reveals a direct band gap ($\sim$0.737 eV at the Γ point) suitable for photovoltaic applications, while the optical spectra confirm strong anisotropic absorption in the visible and ultraviolet regions (exceeding 1.5×10^5 cm^{-1} after 2 eV). Thermoelectric analysis across a broad temperature range yields a figure of merit (zT) approaching 0.88 at 900 K, showing excellent energy conversion potential. Collectively, our comprehensive DFT-based study highlights $CuBiSeCl_2$ as a stable, optically active, and thermoelectrically efficient multifunctional material for next-generation energy harvesting and optoelectronic device integration.

2. Methodology: computational and theoretical framework

2.1. Density functional theory

This study employed first-principles calculations utilizing the full-potential linearized augmented plane wave (FP-LAPW) method[23] within the WIEN2K simulation package.[24] The electronic exchange–correlation effects were addressed through the Generalized Gradient Approximation (GGA) as established by Perdew, Burke, and Ernzerhof for exchange in solids and surfaces (PBESol).[25] Structural optimization was performed using the Broyden–Fletcher–Goldfarb–Shanno (BFGS) minimization scheme, with the total energy convergence and charge convergence criteria set to 10^{-5} Ry and 10^{-4} e, respectively. The q-limit was set to 0.05 for SCF calculation. The wave function cutoff parameter RMT*Kmax was established at 8.0, accompanied by a cutoff energy of −6.0 Ry to avoid overlapping muffin-tin spheres. RMT represents the minimum muffin-tin radius across all atomic spheres. To ensure the reliability of our calculations, we carefully performed a basis set convergence test with respect to the RK_{max} parameter (RMT × R_{max}), as shown in Fig. S1 in SI. In LAPW-based electronic structure computations, G_{max} was set to 12 $Bohr^{-1}$ to establish the cutoffs for Fourier expansion. The chosen specific RMT values for the Cu, Bi, Se and Cl atoms were 2.17, 2.5, 2.07, and 2.0, respectively. The Monkhorst–Pack[26] k-point method was employed for integration of the Brillouin zone. The core and valence electronic configurations utilized in the calculations included Cu ($4s^1$ $3d^{10}$), Bi ($4f^{14}$ $5d^{10}$ $6s^2$ $6p^3$), Se ($3d^{10}$ $4s^2$ $4p^4$), and Cl ($3s^2$ $3p^5$). A 1000 k-point (8 × 19 × 5) mesh grid was used for the configurations. For calculations of density of states (DOS) and optical properties, a denser mesh of 2000 k-points (11 × 24 × 7) was used to ensure higher accuracy. Optical properties were analysed with the OPTIC module.[27] Calculation of thermoelectric transport properties was conducted using the semiclassical BoltzTraP2 code,[28] which was applied after SCF calculation. zT values were obtained under the constant relaxation time approximation (CRTA) using BoltzTraP2 code,[28] where the full phonon-scattering or electron relaxation-time calculations were not considered. The optical properties along the xx- and zz-axes are illustrated in the figure to demonstrate the anisotropic response resulting from the layered octahedral framework. Elastic calculations employed the same parameters as the SCF calculations, with a 5 × 13 × 3 k-point mesh. Structural visualization and analysis were performed using the XCrySDen package[29] and actual crystal drawings were made by utilizing VESTA.[30]

3. Results and discussion

3.1. Structural stability analysis with ground-state properties

$CuBiSeCl_2$, a quaternary halide chalcogenide material (Fig. 1), crystallizes in orthorhombic symmetry with space group *Pnma* (No. 62) and contains a total of 20 atoms per unit cell. Based on

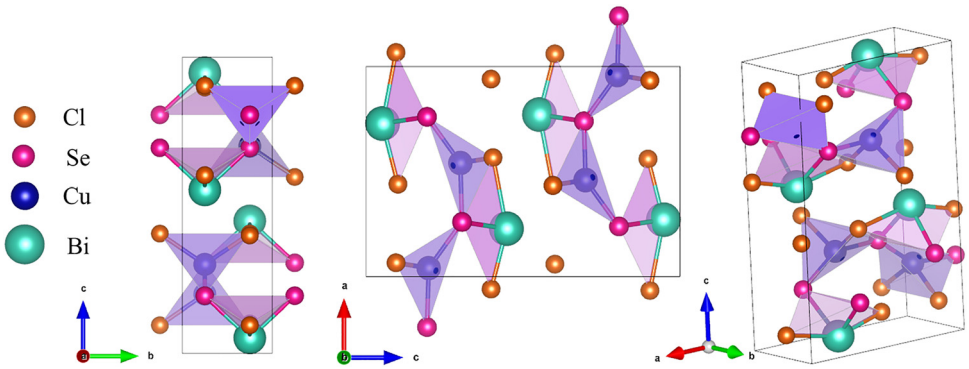

Fig. 1 The 2D and 3D crystal structures of $CuBiSeCl_2$.

Table 1 Atomic positions, isotropic displacement parameters and site occupancy factors[31]

Atom	Oxidation state	Wyck.	x	y	z	Occ.	U_{iso} (Å)
Bi-1	Bi^{3+}	4c	0.265(2)	1/4	0.4495(9)	1.0	0.00595(4)
Se-1	Se^{2-}	4c	0.255(6)	1/4	0.4495(9)	1.0	0.00456(8)
Cu-1	Cu^{+}	4c	0.0324(6)	1/4	0.4495(9)	1.0	0.0443(3)
Cl-1	Cu^{-}	4c	0.059(1)	1/4	0.4495(9)	1.0	0.0038(4)
Cl-2	Cu^{-}	4c	0.44(1)	1/4	0.4495(9)	1.0	0.0139(4)

powder X-ray diffraction analysis conducted by C. J. Hawkins *et al.*,[31] all atoms are found to occupy the 4c Wyckoff position, with corresponding fractional coordinates and equivalent isotropic displacement parameters U_{iso}, while their oxidation states were identified *via* XPS (Table 1).

In order to estimate the equilibrium structural parameters of $CuBiSeCl_2$, we minimized the total energy of the crystal with respect to both atomic positions and cell parameters. By performing volume-dependent total energy calculations and fitting the results with Murnaghan's equation of state,[32] we found that $CuBiSeCl_2$ reaches its lowest energy configuration of −212 638.72847 Ry at a volume of 457.382 a.u.^{3}, as illustrated in Fig. 2(b) and summarized in Table S3. This corresponds to its equilibrium state.

The geometrically optimized lattice parameters are shown in Fig. 2(a) and summarized in Table S4 and compared with previously reported results. It is noteworthy that our calculated values, obtained using the GGA approximation with the PBEsol functional, show good agreement with both experimental and theoretical data. The relative errors with respect to the experimental values are approximately 0.38%, 0.34% and 0.36% for the lattice parameters a, b, and c, respectively.

Formation enthalpy $\Delta H_f(CuBiSeCl_x)$ and cohesive energy $E_{coh}(CuBiSeCl_x)$, were employed as essential thermodynamic descriptors to assess the structural and energetic stability of the quaternary chalcogenide halide $CuBiSeCl_2$, and are defined as follows:[33]

The calculated formation enthalpy of $CuBiSeCl_2$ is −2.751 eV per atom, evidence of its thermodynamic stability against elemental decomposition. In addition, the highly negative cohesive energy of −15.613 eV per atom reflects the presence of strong interatomic interactions that stabilize the crystal framework. These energetic parameters collectively demonstrate the structural robustness of $CuBiSeCl_2$. Thus, the compound exhibits intrinsic thermodynamic stability and potential for practical application. The detailed values of formation enthalpy and cohesive energy are listed in Table S2.

3.2. Electronic properties

A comprehensive understanding of the electronic structure of $CuBiSeCl_2$ is essential for assessing its suitability in photovoltaic, optoelectronic and thermoelectric applications. These calculations were performed using density functional theory (DFT). Analysis of the band structure determines the nature of the band gap and offers critical information regarding the energy dispersion near the Fermi level, which is directly linked to charge carrier mobility and electronic transitions.[34] Furthermore, the total and partial density of states (PDOS) clarify the atomic orbital contributions to the conduction bands and valence bands, highlighting the roles of specific orbitals in bonding, electronic transitions, charge transport, and optical absorption. Fig. 3(a) displays the calculated band structure along high-symmetry directions in the first Brillouin zone, with k-points labeled Γ, X, S, Y, Γ, Z, U, R, T, and Z exhibiting a direct band gap of 0.737 eV at the Γ point, where both the valence band maximum (VBM) and conduction band minimum (CBM) are aligned, confirming the direct nature of the band gap. While DFT calculations employing standard exchange–correlation functionals GGA typically underestimate band gaps, the experimentally observed value of approximately 1.33 eV[31] falls within the desirable range for photovoltaic and optoelectronic devices. The curved bands near the top of the valence band and bottom of the conduction band suggest that the charge carriers

$$\left\{\begin{array}{l}\Delta H_f(CuBiSeCl_x) = \dfrac{E_{tol}(CuBiSeCl_x)) - E_{coh}(Cu) - E_{coh}(Bi) - E_{coh}(Se) - xE_{coh}(Cl)}{5} \\ E_{coh}(CuBiSeCl_x) = \dfrac{E_{tol}(CuBiSeCl_x)) - E_{ios}(Cu) - E_{ios}(Bi) - E_{ios}(Se) - xE_{ios}(Cl)}{5}\end{array}\right\} \quad (1)$$

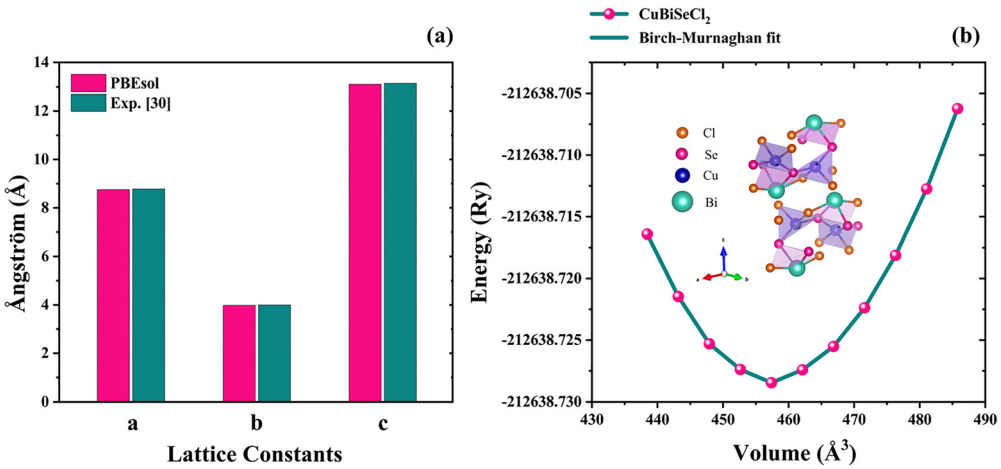

Fig. 2 (a) Optimized lattice constants and (b) the energy *vs.* volume relationship for $CuBiSeCl_2$.

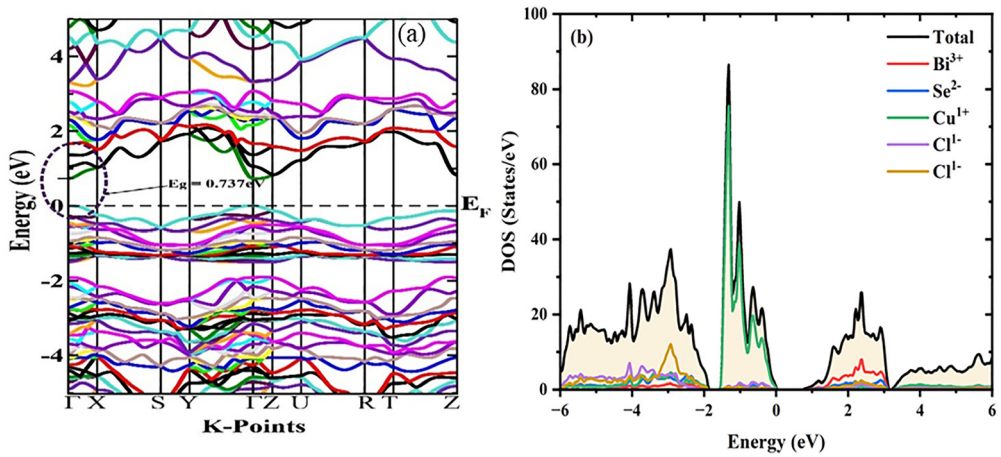

Fig. 3 First-principles results for $CuBiSeCl_2$: (a) electronic band structure and (b) total and partial density of states (TDOS and PDOS).

have low effective mass, which helps improve conductivity and mobility. Flatter bands further away from the Fermi level represent localized electrons, whereas the more spread-out bands near the Fermi level indicate that electrons can move freely, aiding transport. Analysis of the electronic structure indicates that Cu 3d, Se 4p, and Cl 3p states dominate below the Fermi level, whereas Bi 6p orbitals are the primary contributors to the conduction band.

The relationship between orbital interactions and the electronic structure of $CuBiSeCl_2$ can be effectively understood through DOS analysis, which also reflects the optical responses of the material.[35] However, Fig. 3(b) provides a detailed visualization of the total and partial DOS, delineating the orbital-specific contributions of each element. The electronic stability of a compound is often correlated with the TDOS at the Fermi level, where a lower value typically signifies greater thermodynamic stability.[36,37] The electronic states below the Fermi level are largely influenced by the Cu 3d, Se 4p, and Cl 3p orbitals, indicating significant hybridization among these elements in the valence band region. In contrast, the conduction band, located above the Fermi level, is derived primarily from the Bi 6p orbitals, with minor contributions from Se and Cl states. This distribution of electronic states suggests that Cu, Se, and Cl play a dominant role in hole transport, while Bi states are chiefly responsible for electron conduction in $CuBiSeCl_2$. However, a detailed element- and orbital-resolved (s, p, d) PDOS analysis and charge density analysis for Cu, Bi, Se, and Cl are provided in the SI (Fig. S1 and S2), highlighting their individual contributions to the electronic structure.

3.3. Optical properties

The optical characteristics of materials have garnered significant interest in recent years, primarily because of their pivotal role in integrated photonic systems, including optical computing, modulation, optoelectronic devices like photovoltaics, photodetectors, LEDs, and sensors, and high-speed communication.[38,39] These characteristics arise from the interaction between incoming light and the electronic structure of the material, particularly through processes like absorption, reflection, and refraction. In this study, comprehensive optical analysis has been carried

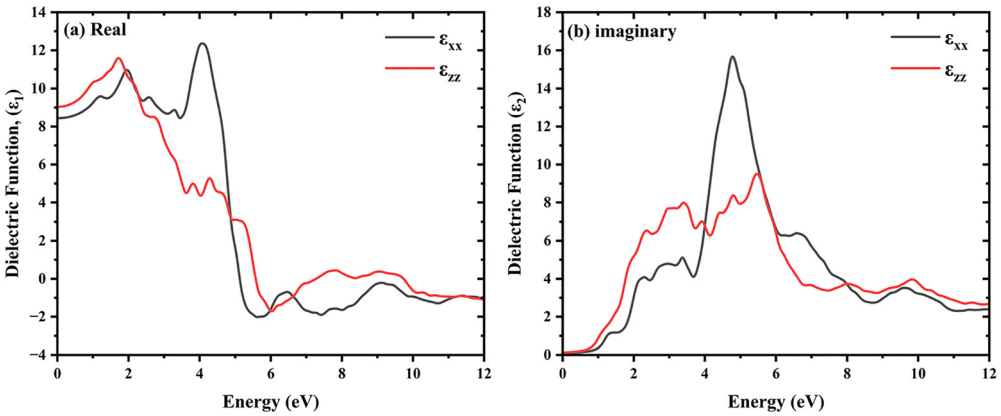

Fig. 4 The calculated (a) real and (b) imaginary components of the dielectric function of $CuBiSeCl_2$ in terms of energy.

out to explore the interaction of $CuBiSeCl_2$ with electromagnetic radiation in the 0–12 eV range, through key parameters including absorption coefficient, reflectivity, refractive index, dielectric constant, optical conductivity, and loss function.

The optical and electronic characteristics of $CuBiSeCl_2$ can be elucidated through the real (ε_1) and imaginary (ε_2) parts of its frequency-dependent dielectric function.[40] Fig. 4 presents the frequency-dependent dielectric function of $CuBiSeCl_2$, highlighting its two independent tensor elements, $\varepsilon_{xx}(\omega)$ and $\varepsilon_{zz}(\omega)$. It is evident that $CuBiSeCl_2$ exhibits static dielectric constants of $\varepsilon_{1_{xx}}(0) = 9.0$ and $\varepsilon_{1_{zz}}(0) = 8.5$ (Fig. 4(a)). At low photon energies, the real part of the dielectric function, $\varepsilon_1(\omega)$, rises sharply and attains distinct maximum peaks: $\varepsilon_{1_{xx}}(\omega)$ peaks at approximately 2.0 eV, while $\varepsilon_{1_{zz}}(\omega)$ displays two notable peaks around 1.8 eV and 4.0 eV. Notably, within the visible energy range, both components show elevated values, reaching 11.0 and 11.9, respectively. Subsequently, the dielectric function values drop steeply, turning negative at around 5.0 eV and 5.5 eV for $\varepsilon_{1_{xx}}(\omega)$ and $\varepsilon_{1_{zz}}(\omega)$, respectively. However, these peaks indicate significant interaction between the incident light and the electronic cloud of the material, enabling energy storage through electric field coupling. The negative values observed in specific energy ranges suggest metallic-like behavior, characterized by high reflectivity, as commonly reported for similar semiconductor systems.[41] The imaginary part of the dielectric function $\varepsilon_2(\omega)$, illustrated in Fig. 4(b), characterizes the optical absorption behavior of $CuBiSeCl_2$, with its onset at around 0.73 eV and 0.74 eV for $\varepsilon_{2_{xx}}(\omega)$ and $\varepsilon_{2_{zz}}(\omega)$, corresponding to the band gap energy and indicating the beginning of photon-induced transitions. The distinct peaks in $\varepsilon_2(\omega)$, are the result of optical transitions between the valence and conduction bands, consistent with the electronic states near the Fermi level.[42]

The absorption coefficient (α) is a wavelength-dependent parameter that indicates how rapidly light intensity diminishes as it propagates through a material. Fig. 5(a) illustrates the absorption coefficient $\alpha(\omega)$ as a function of photon energy, revealing anisotropy between the xx and zz directions. The absorption spectrum is initiated near $\sim$0.8 eV, indicating a direct correlation with its electronic band gap. Here, the initial absorption trend below 2 eV with a moderate slope supports a direct band gap nature, as typically expected in chalcohalide systems.[43,44] Across the 1–12 eV range, α_{xx} remains higher than α_{zz}, indicating strong optical anisotropy, which is a hallmark of non-cubic, layered, or low-symmetry materials.[45] However, the absorption coefficient of $CuBiSeCl_2$ exceeds 1.5×10^5 cm^{-1} after 2 eV, highlighting its potential as an efficient light-harvesting material for solar cell devices. Some major absorption peaks are observed throughout the spectrum. Notably, a

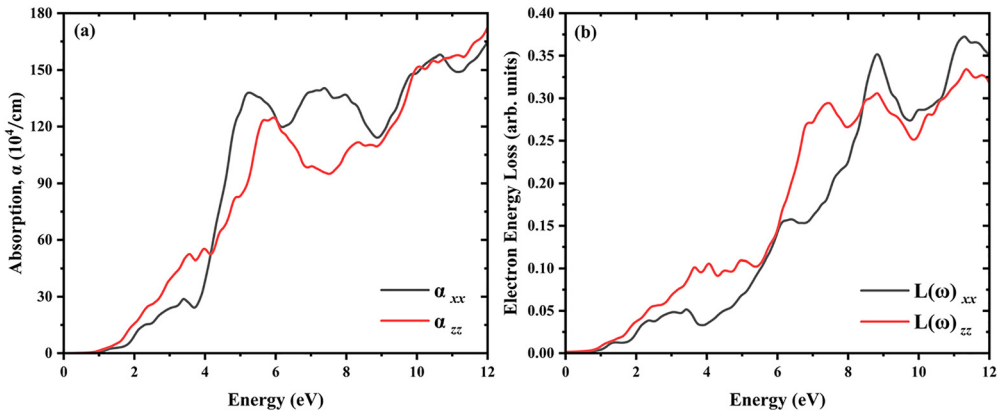

Fig. 5 The calculated (a) absorption and (b) electron energy loss of $CuBiSeCl_2$ as a function of energy up to 12 eV.

strong peak in the range ~3.5–4.5 eV ($\alpha_{xx} > 1.4 \times 10^6$ cm^{-1}) is likely attributable to inter-band transitions from deeper valence states to the conduction band. A second prominent absorption region appears in the range ~5.0–8.5 eV, which is likely to be associated with electronic transitions from Cl/Se hybridized valence states to higher-lying conduction band states.[43] These peaks suggest that $CuBiSeCl_2$ can be efficient for UV and near-UV optoelectronic applications, beyond standard visible-range photovoltaics.

The loss function provides insight into how energetic electrons lose energy through interactions with the electronic structure of a material, with prominent peaks highlighting plasmonic resonances and collective oscillatory modes.[46] The gradual increase in the energy loss function $L(\omega)$ from 0 to ~2 eV suggests Drude-like free-electron behavior or residual low-energy plasmon tailing (Fig. 5(b)). A sharp, dominant peak occurs at ~8.5 eV for $L(\omega)_{xx}$, and slightly lower one for $L(\omega)_{zz}$. This corresponds to the bulk plasmon resonance of the material, arising predominantly from collective oscillations of valence electrons, mainly Se and Cl p-states. After the main peak, $L(\omega)$ shows damped oscillations, reflecting energy loss due to inter-band transitions. These indicate high-energy transition channels, which contribute to dielectric screening and affect optical constants. The optical reflectivity spectrum of $CuBiSeCl_2$ provides critical insight into its ability to interact with and reflect incident electromagnetic radiation across different photon energy ranges. Fig. 6 illustrates the computed reflectivity $R(\omega)$ as a function of photon energy, evaluated along both the in-plane $R(\omega)_{xx}$ and out-of-plane $R(\omega)_{zz}$ directions. At low photon energies, both reflectivity components start around ~0.25 and exhibit modest increases, with the $R(\omega)_{zz}$ component slightly higher than $R(\omega)_{xx}$ up to 3.5 eV, corresponding to a regime where the material exhibits transparency or weak absorption due to photon energies being near or below the band gap. Also, a sharp increase in $R(\omega)_{xx}$ is observed starting at ~3.8 eV, peaking near 5.3 eV with a reflectivity value close to 0.47. This peak corresponds to resonant optical transitions, most likely from Se 4p and Cl 3p valence states to Bi 6p-dominated conduction bands. The higher amplitude of $R(\omega)_{xx}$ relative to $R(\omega)_{zz}$ indicates enhanced in-plane polarizability, likely arising from strong orbital hybridization between Cu–Se and Bi–Cl within the basal plane.[47,48] At photon energies beyond 10 eV, the reflectivity again shows oscillations and secondary peaks around 10.5 eV in both directions, which are possibly induced by deep-level electronic transitions. The distinct reflectivity spectrum of $CuBiSeCl_2$, particularly its strong UV reflectance and spectral valleys, make it a compelling material for UV-sensitive applications and anti-reflection coatings in photovoltaic and optoelectronic interfaces.

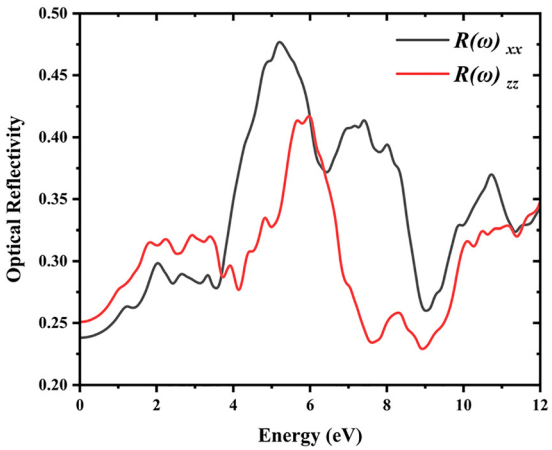

Fig. 6 The calculated reflectivity of $CuBiSeCl_2$ as a function of energy up to 12 eV.

The optical conductivity $\sigma(\omega)$, comprising both real and imaginary parts, provides critical information about the electronic transition dynamics and light–matter interaction strength in a material. Fig. 6(a) highlights the real part of the optical conductivity, which quantifies photon absorption arising from inter-band electronic transitions. At photon energies below ~2.0 eV, both in-plane ($\sigma(\omega)_{xx}$) and out-of-plane ($\sigma(\omega)_{zz}$) optical conductivity of real components remain close to zero, reflecting minimal absorption and confirming the semiconducting nature of $CuBiSeCl_2$. A sharp increase begins around 2.5 eV, with $\sigma(\omega)_{xx}$ peaking at ~4.8 eV (~9.5×10^{15} s^{-1}), driven by direct inter-band transitions. The higher $\sigma(\omega)_{xx}$ suggests in-plane electronic delocalization and strong orbital hybridization. The $\sigma(\omega)_{zz}$ component also rises in this region, peaking at a lower magnitude (~7.5×10^{15} s^{-1}) at ~5.5 eV, indicating a weaker out-of-plane dipole transition, probability due to the reduced orbital overlap in the layered direction. Above 6 eV, both components flatten and gradually decline, with minor oscillations pointing to transitions involving deeper states. This drop reflects reduced optical activity and lower absorption efficiency at high photon energies.

Fig. 7(b) shows the imaginary part of the optical conductivity, which reflects dispersive behavior and phase-shifted current responses. At photon energies below 5.0–5.5 eV, the imaginary part of the optical conductivity, $\sigma(\omega)$ remains negative in both the in-plane ($\sigma(\omega)_{xx}$) and out-of-plane ($\sigma(\omega)_{zz}$) directions, with a distinct dip around 4.2 eV for $\sigma(\omega)_{xx}$. This negative region reflects capacitive behavior, where the material tends to store rather than dissipate energy. As the photon energy increases into the 5.0–5.5 eV range, both components rise sharply, cross into positive values, and enter the resonant dispersion regime. This shift aligns with the onset of significant real conductivity, marking the transition to a more absorptive and optically active state. Beyond 8 eV, the $\sigma(\omega)$ curves gradually level off toward zero in both directions, suggesting a weakening polarization response. The flattening of the response beyond 8 eV indicates that the material becomes less responsive to external fields, consistent with the reduced dielectric contrast and limited excitability of deeper valence electrons.

The optical behavior of a material can be fully described by its complex refractive index, $\tilde{n}(\omega) = n(\omega) + ik(\omega)$, where $n(\omega)$ is the real part (refractive index) describing phase velocity, and $k(\omega)$ is the imaginary part (extinction coefficient), representing attenuation due to absorption. As shown in Fig. 8(a),

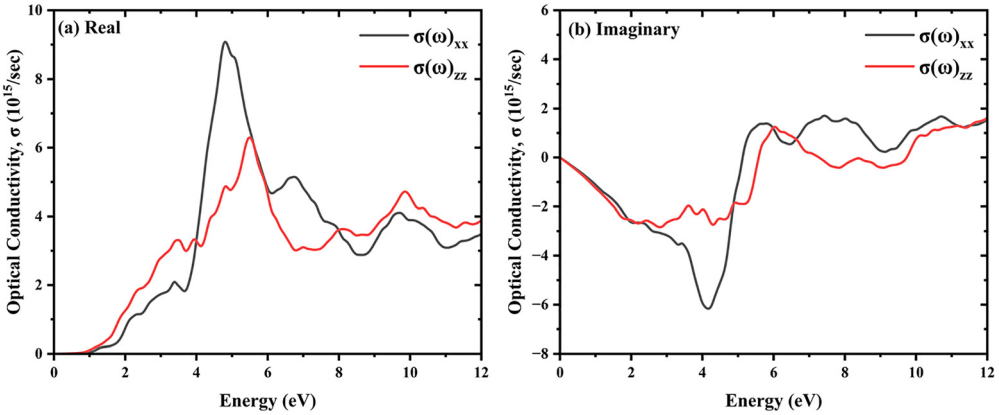

Fig. 7 The computed (a) real and (b) imaginary components of the conductivity of $CuBiSeCl_2$ in terms of energy up to 30 eV.

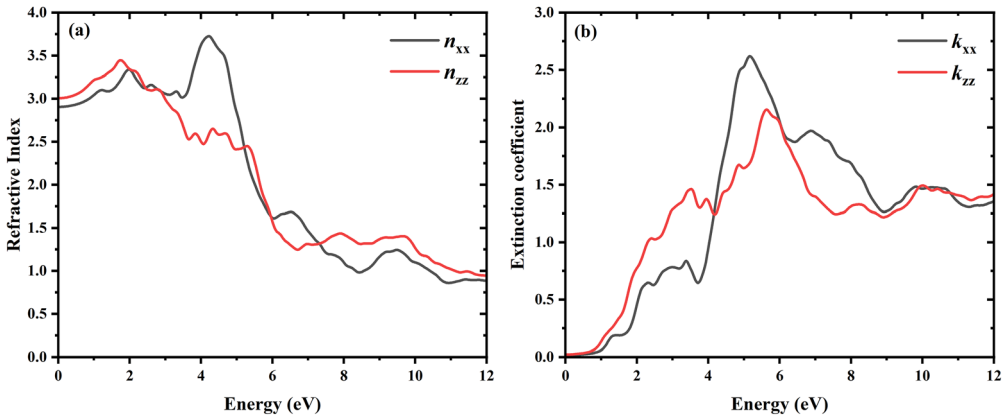

Fig. 8 The computed (a) refractive index and (b) extinction coefficient of $CuBiSeCl_2$ in terms of energy up to 12 eV.

the refractive index exhibits strong energy dependence and pronounced anisotropy between n_{xx} and n_{zz}. In the infrared to visible range (0–3 eV), both n_{xx} and n_{zz} display high values: ~3.45 and ~25, respectively. Such behavior reflects strong optical coupling and reduced light velocity, driven by electronic polarizability. This is common in materials with small band gaps and heavy atomic masses. These properties make them suitable for high-refractive-index applications like waveguides, optical coatings, and transparent electronics. Around 3–6 eV, n_{xx} rises sharply, reaching a maximum of ~3.8 near 4.25 eV, reflecting resonant dispersion effects from inter-band absorption. This observed dispersion behavior aligns well with the strong peaks seen in the optical conductivity and extinction coefficient spectra. Beyond 6 eV, both n_{xx} and n_{zz} decrease gradually and approach ~1.25 at around 11 eV. This reduction indicates a transition to a transparent or weakly absorbing state, where dielectric contributions diminish and light propagation becomes less dispersive.

The extinction coefficient $k(\omega)$, shown in Fig. 8(b), reveals key insights into the optical absorption behavior of the material. Below 2 eV, both k_{xx} and k_{zz} remain near zero, indicating negligible absorption and supporting the presence of a semiconducting nature. A sharp increase in absorption begins around 2.0 eV, with prominent peaks at ~5.2 eV for k_{xx} and ~5.8 eV for k_{zz}, corresponding closely with features observed in the optical conductivity and reflectivity spectra. These peaks arise from strong direct inter-band transitions, mainly involving p/d orbital contributions from the valence band to empty conduction states. The higher intensity in k_{xx} compared to k_{zz} reflects anisotropic absorption, where in-plane light propagation leads to more efficient electronic transitions. Beyond 6 eV, the extinction coefficient gradually declines, indicating reduced absorption due to fewer available states or forbidden transitions an observation that aligns with the drop in the real part of the optical conductivity $\sigma(\omega)$.

3.4. Thermoelectric characteristics

We present a comprehensive evaluation of the thermoelectric transport properties of our target material at a fixed chemical potential μ = 0.204, across a wide temperature range (100–900 K). The calculated quantities, such as electronic thermal conductivity (k_e/τ_0), specific heat (C_V), Seebeck coefficient (S), electrical conductivity (σ/τ), power factor ($S^2\sigma/\tau$), and figure of merit (zT), are depicted in Fig. 9(a–f). Thermal conductivity (k) measures the ability of a material to conduct heat. The overall thermal conductivity in thermoelectrics comes from two terms:

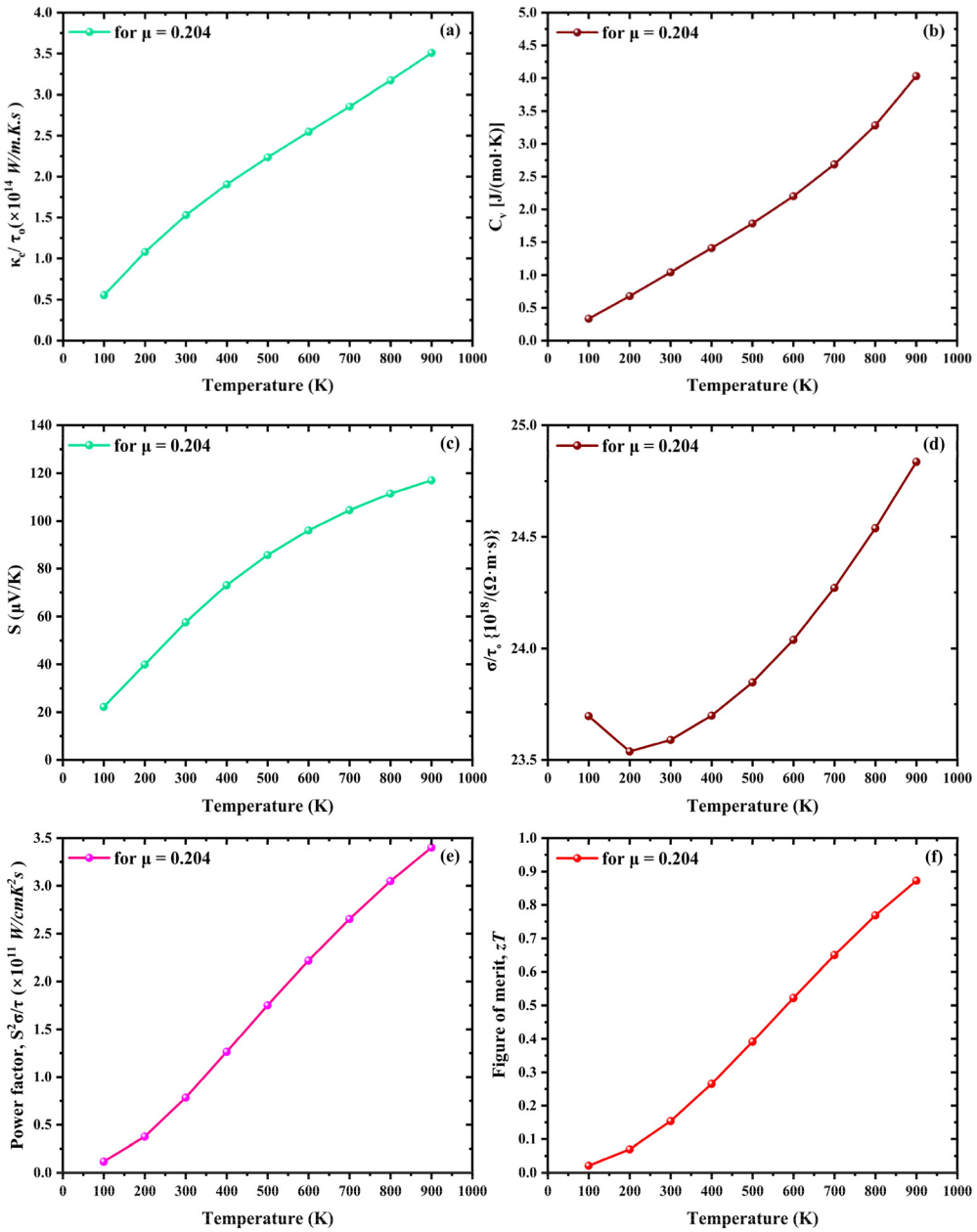

Fig. 9 Calculated (a) electronic thermal conductivity (k_e/τ_0), (b) specific heat (C_V), (c) Seebeck coefficient (S), (d) electrical conductivity (σ/τ), (e) power factor ($S^2\sigma/\tau$), and (f) figure of merit (zT) of $CuBiSeCl_2$ in terms of temperature from 100 K to 900 K.

(i) electronic thermal conductivity (k_e) and (ii) lattice thermal conductivity (k_L) stemming from phonon transport and overall thermal conductivity, which depends largely on electronic conductivity, carrier concentration, and mobility. WIEN2k itself does not compute the lattice thermal conductivity (k_L). Hence, effectively, the lattice channel is not evaluated in our calculations (often shown as $k_L = 0$ by default in the transport module output). This is because the Wiedemann–Franz law connects the electronic part of the thermal conductivity (k_e) to the electronic conductivity (σ). The σ also correlates with carrier concentration (n) and carrier mobility (μ). According to the Wiedemann–Franz law, overall thermal conductivity can be calculated with the following equation:[49]

$$\begin{aligned} k &= k_e + k_L \\ k_L &= 0 \\ k_e &= \sigma L T \\ \sigma &= ne\mu \\ k &= k_e = ne\mu L T \end{aligned} \quad (2)$$

where k is the overall thermal conductivity (*i.e.*, electronic thermal conductivity, W m^{-1} K^{-1}), L is the Lorenz factor

(2.4×10^{-8} J^2 K^{-2} C^{-2} for free electrons), σ is the electrical conductivity (S m^{-1}), n is the majority carrier concentration (m^{-3}), e is the elementary charge (1.6×10^{-19} C), and μ is the carrier mobility (m^2 V^{-1} s^{-1}).

Fig. 9(a) illustrates a steady and nonlinear increase in k_e/τ_0 from approximately 0.6×10^{14} W m^{-1} K^{-1} s^{-1} at 100 K to about 3.6×10^{14} W m^{-1} K^{-1} s^{-1} at 900 K. At low temperatures ($T <$ 200 K), the electronic thermal conductivity is relatively low. This is due to the limited thermal excitation of carriers across the band structure. In this regime, the electronic contribution to thermal transport is typically minor compared to that of lattice thermal conductivity. As temperature increases, a larger number of carriers are thermally excited. These carriers can carry both charge and heat, leading to an enhanced electronic thermal conductivity. The behavior of k_e/τ_0 observed here aligns well with known semiconductors and thermoelectric materials, such as Cs_2BiAgX_6 (X = Cl, Br)[50] or $BiSbSeTe_2$,[51] where the electronic contribution to thermal conductivity increases with temperature due to carrier excitation and band convergence. The heat capacity is a fundamental thermodynamic property that plays a key role in determining its energy storage ability, thermal conductivity, and behavior under thermal gradients. A high C_V at the operating temperature is desirable in some thermoelectrics because it helps buffer against large thermal fluctuations and can moderate local overheating.

Fig. 9(b) shows the calculated variation in the heat capacity at constant volume, C_V, which reveals a smooth, monotonically increasing trend, starting from approximately 0.3 J mol^{-1} K^{-1} at low temperatures and rising to approximately 4.1 J mol^{-1} K^{-1} at 900 K. In the low-temperature regime (100–300 K), the curve shows a gentle initial rise, with values increasing from $\sim$0.3 J mol^{-1} K^{-1} to $\sim$1.0 J mol^{-1} K^{-1}, which is typical for non-degenerate semiconductors, where only a small number of charge carriers near the Fermi level are thermally active. This slow rise confirms the lack of metallic behavior and suggests a relatively low DOS near the Fermi level. However, the heat capacity increases more rapidly, climbing from $\sim$1.0 to $\sim$3.0 J mol^{-1} K^{-1} in the intermediate temperature regime (300–700 K). This behavior reflects that the material is transitioning into a regime where entropy per carrier becomes significant, which is favorable for thermoelectric performance. In the high-temperature regime (700–900 K), C_V continues to rise steeply, reaching $\sim$4.2 J mol^{-1} K^{-1} at 900 K, suggesting strong carrier delocalization and dispersion. Although phonon contributions are not included, the electronic C_V is critical for modeling energy-dependent transport properties and optimizing performance.

The Seebeck coefficient S, quantifies the voltage generated per unit temperature difference in a material and arises due to the entropy carried by charge carriers. Fig. 9(c) presents the temperature dependence of the Seebeck coefficient S, highlighting a steady and nonlinear increase from $\sim$24 μV K^{-1} at 100 K to $\sim$118 μV K^{-1} at 900 K, indicating favorable thermoelectric potential and a clear signature of the underlying carrier type and band structure. At low temperatures (100–300 K), S increases moderately from $\sim$24 to $\sim$60 μV K^{-1}. The small value of S at 100 K indicates a high carrier concentration or narrow band offset between μ and the VBM. However, the linear growth in this region is governed by Mott's formula:[52]

$$S = \frac{\pi^2 k_B^2 T}{3e}\left(\frac{d \ln \sigma(E)}{dE}\right)_{E=\mu}$$

This shows that $S \propto T$ if $\sigma(E)$ is slowly varying, which aligns with the observed trend.

From 300 K to 700 K, S increases more rapidly, reaching $\sim$100 μV K^{-1}. The nonlinear increase in this region implies the presence of complex band features (*e.g.*, secondary valleys) contributing to transport, which is desirable for thermoelectric performance. In the high-temperature regime, the Seebeck coefficient reaches its maximum value of $\sim$128 μV K^{-1} at 900 K. This behavior highlights the thermoelectric suitability of the material at elevated temperatures. In many semiconductors, S tends to saturate or even decrease at high T due to bipolar diffusion effects.[53,54] The absence of this downturn suggests that the chemical potential shifts with T (as BoltzTraP allows), keeping minority carrier effects minimal.[55] Fig. 9(d) depicts the calculated temperature-dependent electrical conductivity, where it initially exhibits a weak decline, reaching a minimum around 200 K, followed by a systematic and nonlinear increase up to 900 K. In the 100–200 K range, σ/τ slightly decreases, reaching a local minimum at $\sim$200 K. This weak dip can be attributed to reduced thermal excitation, as at the low temperature, fewer states near the Fermi level contribute to conduction.[56] Also, if the Fermi level lies close to the band edge, the density of thermally excited carriers is limited. After reaching the minimum, σ/τ increases gradually, indicating the activation of additional carriers with temperature in the range of 200–600 K. This trend suggests that the system transitions from weakly conducting to strongly conducting, a hallmark of semiconductors with thermally activated transport. Beyond 600 K, the conductivity increases more sharply, reaching approximately 25×10^{18} (Ω m s)$^{-1}$ at 900 K. This suggests that the carrier concentration increases significantly due to thermal excitation deeper into the valence band. However, these findings support a strong power factor and a high figure of merit, as analyzed in the next sections.

The power factor is a critical metric in thermoelectric research because it determines the electrical contribution to the thermoelectric efficiency, independent of thermal conductivity. Fig. 9(e) illustrates the temperature dependence of the power factor and reveals a steady and nearly exponential increase in PF from $\sim 0.1 \times 10^{11}$ to $\sim 3.4 \times 10^{11}$ over the temperature range 100–900 K. In the range from 100 K to 500 K, the PF increases moderately from $\sim$0.1 to $\sim$1.3 ($\times 10^{11}$ W m^{-1} K^{-2} s^{-1}). This growth is driven by gradual increases in both S and σ. This region represents the transition from low-mobility behavior to a more active transport regime, indicative of semiconducting transport mechanisms. Beyond 500 K, the PF grows more rapidly, reaching $\sim$3.3 by 900 K. This nonlinear increase suggests that the material benefits from favorable band structure characteristics, such as heavy and

light band mixing. A rising power factor with temperature is highly desirable for high-temperature thermoelectric applications, such as waste heat recovery. An ideal thermoelectric material maintains high PF at elevated temperatures without incurring severe losses in conductivity or saturation in the Seebeck coefficient. Moreover, the absence of PF degradation at 900 K confirms the stability of electronic structure and resistance to bipolar conduction, both of which are vital for practical high-temperature applications. The figure of merit is a comprehensive descriptor that quantifies the overall efficiency of a thermoelectric material in converting heat into electricity, or *vice versa*. Fig. 9(f) illustrates the temperature-dependent behavior of the thermoelectric figure of merit, zT, which shows a steadily increasing trend with temperature. In the lower temperature range (100–300 K), zT remains modest, ranging from ~0.03 to ~0.18, as both the Seebeck coefficient and electrical conductivity are relatively low at these temperatures due to limited thermal excitation of carriers. From 300 K to 600 K, zT increases more noticeably, rising from ~0.18 to ~0.52. This improvement arises from the enhanced carrier activation, which increases both S and σ, as discussed earlier. However, the most significant improvement in performance occurs in the 600–900 K range, where zT increases from ~0.52 to ~0.88. All these zT values are estimated under the constant relaxation time approximation (CRTA) and do not include full phonon scattering or electron relaxation-time calculations. They should be considered as qualitative trends indicative of the thermoelectric potential of the material. However, this high-temperature behavior is critical, as many thermoelectric generators operate under large thermal gradients and require materials that can maintain stability and efficiency under thermal stress. These results position our studied material ($CuBiSeCl_2$) as a strong candidate for high-performance thermoelectric applications, particularly in waste heat recovery, concentrated solar thermoelectrics, and industrial power generation systems.

3.5. Elastic characteristics, and mechanical stability of $CuBiSeCl_2$

The mechanical strength and elastic behavior of a crystalline material under various stress conditions are governed by its elastic constants C_{ij}, which form the stiffness tensor. These constants are pivotal for understanding how a material deforms under applied stress and provide insight into its structural integrity and interatomic bonding. In orthorhombic crystalline systems, nine independent elastic constants: C_{11}, C_{12}, C_{13}, C_{22}, C_{23}, C_{33}, C_{44}, C_{55}, and C_{66}, describe the mechanical response along different crystallographic directions. These parameters are not only critical for evaluating thermal expansion and structural stability, but also offer deeper understanding of interatomic force strengths, bonding anisotropy, mechanical anisotropy, and other physical properties. Moreover, they serve as the basis for calculating key thermomechanical quantities. Such as the Debye temperature, specific heat capacity, thermal conductivity, phonon dispersion, and interatomic potentials.[57]

The elastic constants of $CuBiSeCl_2$ at equilibrium were computed using density functional theory (DFT) and are presented in Fig. 10(a) and Table 2. The principal stiffness coefficient C_{11} measures the resistance to stress along the x-direction.[58] C_{33} reflects the response to stress along the z-axis, while C_{44} corresponds to resistance against shear in the yz-plane. The off-diagonal constants, such as C_{13}, C_{23} and C_{12}, illustrate inter-plane coupling and the degree of anisotropy. To assess the mechanical stability of $CuBiSeCl_2$ under ambient pressure, the Born stability criteria for orthorhombic systems are applied:[59,60]

$$\left\{\begin{array}{c} C_{11}>0; C_{22}>0; C_{33}>0; \\ C_{44}>0; C_{55}>0; C_{66}>0; \\ [C_{11}+C_{22}+C_{33}+2(C_{12}+C_{13}+C_{23})]>0; \\ (C_{11}+C_{33}-2C_{12})>0; \\ (C_{11}+C_{33}-2C_{13})>0; \\ (C_{11}+C_{33}-2C_{23})>0 \end{array}\right\}$$

All these conditions are satisfied by our computed values, confirming the mechanical stability of $CuBiSeCl_2$ in its ground-state configuration. A high C_{11} value reflected by the investigated material suggests strong resistance to uniaxial compression along

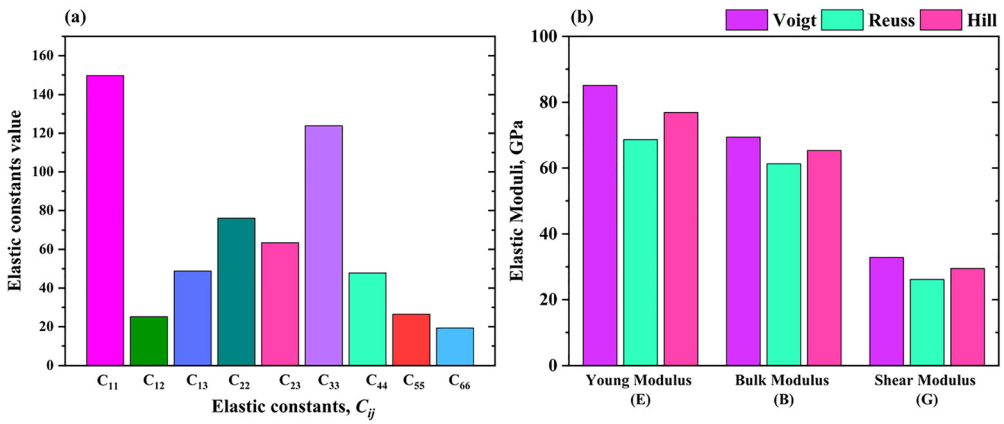

Fig. 10 Calculated (a) elastic constants and (b) elastic moduli of $CuBiSeCl_2$.

Table 2 Nine independent elastic constants of $CuBiSeCl_2$

	Nine independent elastic constants								
Material	C_{11}	C_{12}	C_{13}	C_{22}	C_{23}	C_{33}	C_{44}	C_{55}	C_{66}
$CsGeIBr_2$	149.70	25.17	48.82	76.18	63.49	123.91	47.83	26.45	19.30

the principal crystallographic axis, indicating the stiffness of the material in that direction. Likewise, an elevated C_{44} denotes greater resistance to shear stress, suggesting good rigidity against angular deformation. Conversely, a relatively low C_{12} implies increased lateral flexibility, making the material more compliant under transverse loads, an advantageous property for applications demanding elastic adaptability.

The summarized elastic stiffness parameters of $CuBiSeCl_2$ are presented in Table 3 and Fig. 10(b). The bulk modulus (B), shear modulus (G), and Young's modulus (E) were calculated using the Voigt–Reuss–Hill (VRH) averaging scheme,[61–63] which provides a reliable estimate for polycrystalline materials. The bulk modulus represents the resistance of the material to uniform compression. Higher B values correspond to lower compressibility, indicating stronger atomic cohesion and bonding strength.[64,65] Additionally, the elastic modulus helps to determine atomic cohesion and binding energy, which are key factors in understanding the stability of a material. The shear modulus (G), which quantifies the resistance to shape deformation at constant volume, has a relatively low value compared to the other two moduli, as indicated in Table 3 and Fig. 10(b). Again, the G value is notably smaller than B, implying that shear deformation is more favorable than volumetric compression. This predisposition to shear facilitates dislocation motion within the crystal lattice, increasing the likelihood of plastic deformation under mechanical stress.[66] Young's modulus (E), which measures the stiffness of the material along its length under uniaxial compression, is higher among the three. Nonetheless, the positive values of all three moduli (B, G, and E) indicate that $CuBiSeCl_2$ is mechanically and dynamically stable under ambient conditions.

The Poisson ratio (ν) for $CuBiSeCl_2$ was calculated to be 0.304, which is slightly above the commonly accepted brittle-to-ductile threshold of 0.26 (Fig. 11(a)). Values below 0.26 typically indicate brittle behavior, while values above suggest ductility.[67]

Table 3 Mechanical characteristics of absorber $CuBiSeCl_2$

Mechanical characteristics	Voigt	Reuss	Hill
Young's modulus (E)	85.163	68.640	76.925
Bulk modulus (B)	69.419	61.290	65.354
Shear modulus (G)	32.868	26.132	29.500
Poisson ratio	0.295	0.313	0.304
Pugh ratio	2.215		
Frantsevich ratio (G/B)	0.451		
Transverse elastic wave velocity	2191.71 m s^{-1}		
Longitudinal elastic wave velocity	4128.75 m s^{-1}		
Averaged wave velocity	2449.28 m s^{-1}		
Machinability index (μ_m)	1.37		
Kleinmann parameter (ζ)	0.320		
Lamé coefficient (λ)	45.75		
Debye temperature	257.001 K		

Since ν is above the threshold, $CuBiSeCl_2$ may exhibit ductility, meaning it has the capacity for plastic deformation, but remains relatively stiff under stress. The Pugh ratio (B/G), calculated to be 2.215, exceeds the critical value of 1.75,[68] classifying $CuBiSeCl_2$ as a ductile material according to Pugh's criterion. The Frantsevich ratio (G/B)[69] further supports this classification, as its value is below the critical threshold of 0.57, reinforcing the conclusion that $CuBiSeCl_2$ behaves as a ductile material.

The Kleinman parameter (ζ) provides critical understanding of the internal response of the crystal lattice under volume-conserving deformation. It reflects the competition between bond bending and bond stretching within the crystal. Theoretically, ζ ranges between 0 and 1, where values closer to 0 indicate that bond stretching dominates, while values near 1 suggest that bond bending is more prevalent.[70] In this study, the calculated ζ value for $CuBiSeCl_2$ is 0.320, implying a predominant bond-stretching character under applied strain, which contributes to the mechanical stability of the material against bending distortions. The machinability index (μ_m) is an important industrial metric indicating how easily a material can be cut or shaped without extensive wear or energy consumption. For reference, aluminum, known for its softness and ease of machining, has a high machinability index of around 2.6, while diamond, the hardest known material, has a much lower index of approximately 0.8.[71] For $CuBiSeCl_2$, the calculated value of 1.37 falls in a moderate range, suggesting that the material possesses reasonable plastic deformability and cutting efficiency. This makes it a promising candidate for applications requiring mechanical processing or shaping, particularly in optoelectronic devices and thin-film technologies.

The Lamé coefficient (λ) is another elastic parameter that helps describe how a material resists volume changes when subjected to hydrostatic stress. It combines both bulk and shear moduli contributions to capture the overall stiffness. The obtained λ value of 45.75 GPa for $CuBiSeCl_2$ reflects resistance to volumetric deformation, aligning with the observed values of bulk and shear moduli discussed earlier. Furthermore, the elastic Debye temperature was calculated to be 257.001 K. This parameter relates to the lattice vibration and heat capacity and is useful for evaluating thermal transport and dynamic stability. Wave velocity analysis, including the transverse elastic wave velocity, longitudinal wave velocity, and average wave velocity (2449.28 m s^{-1}), presented in Table 3 and Fig. 11(b), further supports the intermediate stiffness and sound propagation characteristics of $CuBiSeCl_2$.

3.6. Hardness and anisotropy of $CuBiSeCl_2$

To further evaluate the resistance of the material to localized plastic deformation, the Vickers hardness of $CuBiSeCl_2$ was estimated using Chen's empirical model,[72] which relates hardness to the bulk modulus (B) and shear modulus (G). The calculated hardness values are summarized in Table 4. This value suggests that the material is soft and easily machinable, making it potentially suitable for applications requiring moderate wear resistance and mechanical workability, such as in

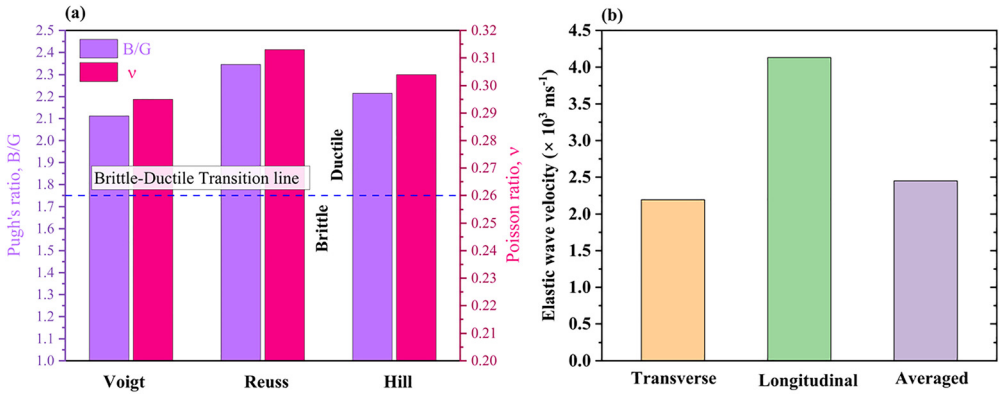

Fig. 11 Calculated (a) Pugh ratio (B/G) and (b) Poisson ratio (ν) of $CuBiSeCl_2$.

Table 4 Hardness of absorber $CuBiSeCl_2$

	Vickers hardness							
Material	H_1	H_2	H_3	H_4	H_5	H_6	H_7	H_8
$CsGeIBr_2$	6.29	4.67	4.35	4.88	2.32	3.28	3.86	2.71

optoelectronic devices or layered device architectures where mechanical processing is necessary.

The universal anisotropy index (A^U) was found to be 1.421. Generally, $A^U = 0$ represents a perfectly isotropic material, while any non-zero value indicates elastic anisotropy.[73] Thus, $CuBiSeCl_2$ exhibits a noticeable degree of anisotropic mechanical behavior, meaning its elastic response varies with direction. In addition to the universal anisotropy index, several other anisotropy indicators were also evaluated for $CuBiSeCl_2$, including the shear anisotropy factor (A^G), bulk anisotropy factor (A^B), equivalent Zener anisotropy factor (A^{eq}), and the log-Euclidean anisotropy index (A^L) and these are listed in Table 5.

The values of A^G and A^B range from 0 to 1, where 0 indicates perfect isotropy and 1 indicates complete anisotropy.[73] In our study, $CuBiSeCl_2$ showed $A^G = 0.114$ and $A^B = 0.062$, suggesting anisotropy but very near to isotropy in shear and bulk responses. The directional shear anisotropy factors, A_1, A_2 and A_3, representing the anisotropy of shear in the (100), (010), and (001) crystallographic planes, respectively, were also computed. These parameters help identify the directional dependence of shear stiffness in different planes. For $CuBiSeCl_2$, the calculated values were $A_1 = 1.087$, $A_2 = 1.447$, and $A_3 = 0.440$, indicating that shear deformation is not uniform across all planes, with slightly higher resistance in the (010) plane compared to the (100) and (001) planes. This further supports the presence of anisotropic mechanical behavior in the crystal. The log-Euclidean anisotropy index (A^L) varies between 0 and 10.27, where a value of 0 denotes isotropic behavior and larger values imply higher anisotropy. For $CuBiSeCl_2$, the calculated value $A^L = 6.682$ reflects moderate anisotropy. Moreover, the equivalent Zener anisotropy factor (A^{eq}) provides a generalized measure of anisotropy across crystal systems, with $A^{eq} = 2.831$ for the current material, reinforcing the directional dependence of its mechanical response. When the anisotropy index $A^z = 1$, the material is considered elastically isotropic. Any deviation from unity denotes anisotropic nature, which is evident in $CuBiSeCl_2$, based on the calculated indices.

To better understand the mechanical anisotropy and spatial dependence of elastic properties of $CuBiSeCl_2$, five key elastic parameters such as Young's modulus (E), shear modulus (G), Poisson ratio (ν), Vickers hardness (H), and bulk modulus (B) are illustrated in Fig. 10 using MATLAB code.[74] These spatial distributions of elastic parameters exhibit deviations from spherical symmetry, indicative of anisotropic behavior and show elongation or flattening in specific directions, confirming that $CuBiSeCl_2$ does not behave uniformly under mechanical loading. From Fig. 12(a), the surface for the Young's modulus (E) exhibits significant anisotropy, with maximum stiffness observed ($\sim$130 GPa) along intermediate directions between [001] and [010], while minimum stiffness ($\sim$60 GPa) appears near the [100] direction. This anisotropy implies that $CuBiSeCl_2$ exhibits direction-dependent resistance to mechanical deformation. The anisotropic nature of G (Fig. 12(b)) reflects the ability of the material to resist shear deformation in various directions and the lowest values ($\sim$20 GPa) are found along off-axis orientations, indicating relatively easier shear deformation in these directions. Fig. 12(c) illustrates the directional behavior of the Poisson ratio ν, ranging from $\sim$0.20 to $\sim$0.45, with a maximum value $\sim$0.45 along directions near [001], while the minimum value $\sim$0.20 appears along off-axis directions. This moderate anisotropy implies that $CuBiSeCl_2$ shows a non-uniform volume change response when strained along different directions. Fig. 12(d) presents strong anisotropy of Vickers hardness H, meaning that the resistance of the material to indentation or scratching changes greatly with direction. Harder orientations

Table 5 The Reuss and Voigt values of C_{44}^R and C_{44}^V in GPa and various anisotropy indicators (A^U, A^Z, A^{eq}, A^G, A^B, and A^L) of $CuBiSeCl_2$

	Anisotropy Indicators										
Material	C_{44}^R	C_{44}^V	A^U	A^Z	A^{eq}	A_1	A_2	A_3	A^G	A^B	A^L
$CsGeIBr_2$	17.57	0.89	1.42	0.77	2.83	1.09	1.45	0.44	0.12	0.06	6.68

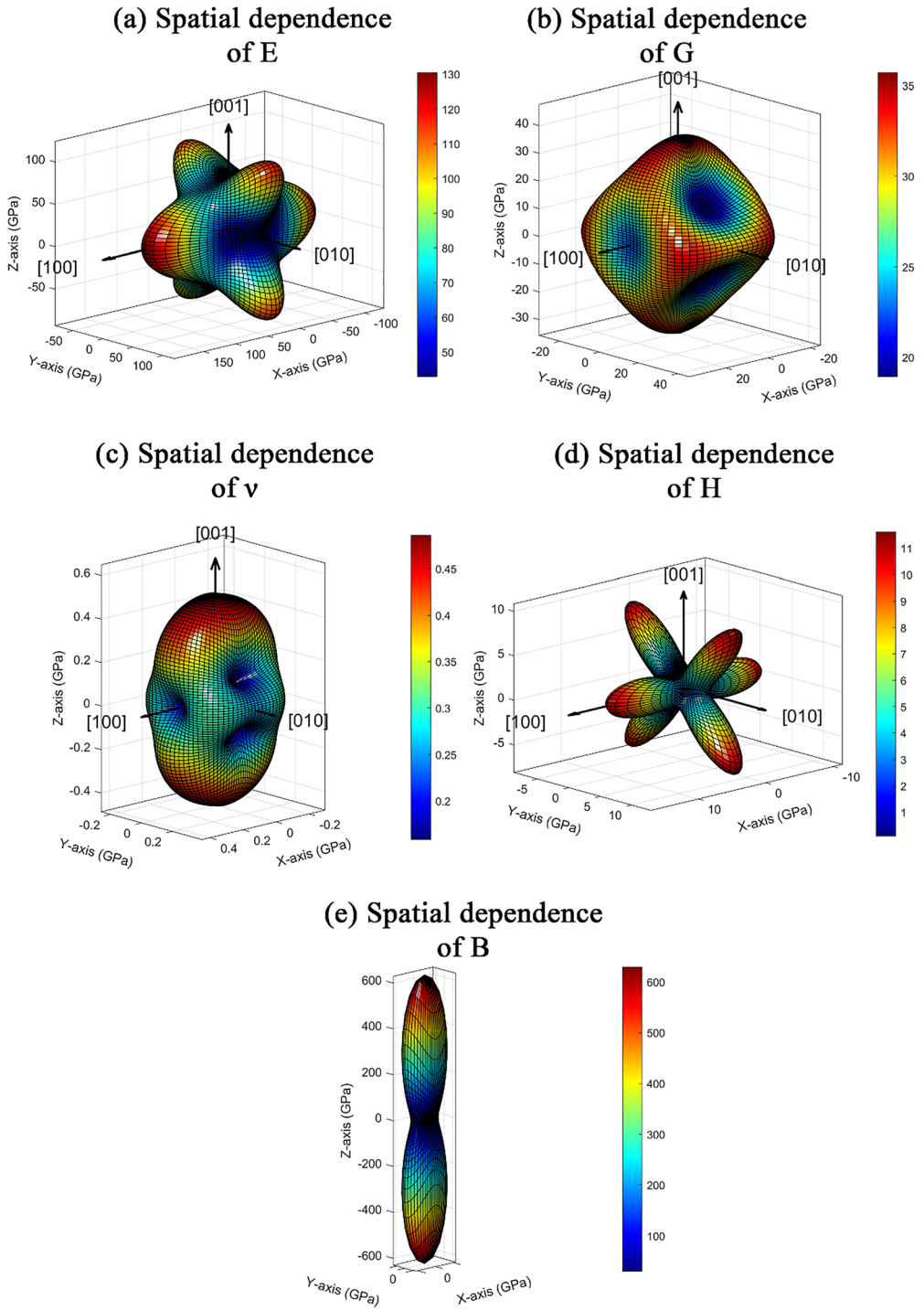

Fig. 12 3D representations of the spatial dependence of anisotropic properties (a)–(e) of $CuBiSeCl_2$.

(around 11 GPa) appear along certain diagonal planes, while much softer responses (~1 GPa) are observed in other orientations. This sharp contrast suggests that the resistance of the material to plastic deformation is highly orientation-dependent. Interestingly, the bulk modulus B shown in Fig. 12(e) exhibits an elongated shape, with extreme values reaching ~600 GPa along the [001] direction and negative or near-zero values in perpendicular directions. This unusual directional variation suggests a highly anisotropic compressibility response, possibly linked to layered bonding and crystallographic symmetry effects.

3. Future plans

The primary aim of this study is to conduct a first-principles investigation of the electronic structure, optoelectronic

potential, and overall thermoelectric trends of $CuBiSeCl_2$ under different carrier concentrations, and our studies will focus on full phonon transport calculations using BTE to obtain precise lattice thermal conductivity and refined zT values, as well as electron relaxation-time modeling for more accurate thermoelectric predictions.

4. Conclusions

This comprehensive investigation identifies $CuBiSeCl_2$ as a mechanically stable, optically active and thermoelectrically efficient quaternary halide chalcogenide, integrating advantageous characteristics for thermoelectric and photovoltaic energy applications. The material has a direct band gap of about 0.737 eV (exp. 1.33 eV) and strong orbital hybridization, revealing its potential for efficient electronic transition and high carrier mobility. Optical property analysis shows strong anisotropic absorption in the visible to ultraviolet range (1.5×10^5 cm^{-1} above 2 eV) with a high refractive index at around 3.8 at 4.25 eV. These show that it can be used in waveguides, optical coatings, and transport engineering. The analysis of thermoelectric transport shows that the Seebeck coefficient, electrical conductivity, and power factor all go up with temperature. At 900 K, the figure of merit is about 0.88, making it a good candidate for high-temperature waste heat recovery and concentrated solar thermoelectric generators. From our investigation, the VRH-averaged elastic characteristics, together with a Poisson ratio that is above the brittle-ductile threshold and a Pugh ratio that is above the critical limit, show that it is moderately ductile and can handle mechanical failure under stress. Significant elastic anisotropy and a Debye temperature of 257 K indicate a modifiable phonon spectrum favorable for thermal transport engineering. Taken together, these findings position $CuBiSeCl_2$. As a promising, environmentally benign material for integration into advanced energy conversion and harvesting systems, such as thermoelectric generators, solar cells, photodetectors, and other optoelectronic devices.

Conflicts of interest

The authors declare that they have no known competing financial interests or personal relationships that could have influenced the work reported in this paper.

Data availability

Data will be made available on request.

Supplementary information (SI) is available. See DOI: https://doi.org/10.1039/d5ma01386k.

Acknowledgements

The authors would like to express their gratitude to Research and Technology Transfer Cell, Pabna University of Science and Technology (PUST), Bangladesh, and the Computational Materials Research Laboratory (CMRL), Department of Physics, PUST, for their partial financial support during this research. Grant number: PUST-RTTC-Project-2025-July-50/108.

References

1 T. Wang, T. Huo, H. Wang and C. Wang, Quaternary chalcogenides: Promising thermoelectric material and recent progress, *Sci. China Mater.*, 2020, **63**, 8–15, DOI: 10.1007/s40843-019-9467-2.

2 D. M. Rowe, *Thermoelectrics handbook: macro to nano*, CRC press, 2005. https://books.google.com/books?hl=en&lr=&id=VvCb_deT4kIC&oi=fnd&pg=PR31&dq=D.M.+Rowe,+Thermoelectrics+handbook:+macro+to+nano,+CRC+press,+2005.&ots=wFv-Qa8b62&sig=WlJNbQkLH8E0nWAZ9pi4yv4tdYo (accessed August 7, 2025).

3 R. P. Chasmar and R. Stratton, The Thermoelectric Figure of Merit and its Relation to Thermoelectric Generators, *J. Electr. Control*, 1959, **7**, 52–72, DOI: 10.1080/00207215908937186.

4 T. Zhu, Y. Liu, C. Fu, J. P. Heremans, J. G. Snyder and X. Zhao, Compromise and Synergy in High-Efficiency Thermoelectric Materials, *Adv. Mater.*, 2017, **29**(30), 1605884, DOI: 10.1002/adma.201605884.

5 H. R. Aliabad, M. Ghazanfari, I. Ahmad and M. A. Saeed, *Ab initio calculations of structural, optical and thermoelectric properties for CoSb3 and ACo4Sb12 (A= La, Tl and Y) compounds*, Elsevier, 2012. https://www.sciencedirect.com/science/article/pii/S0927025612005058 (accessed July 18, 2025).

6 K. Yuan, Z. Sun, X. Zhang, X. Gong and D. Tang, A first-principles study of the thermoelectric properties of rhombohedral GeSe, *Phys. Chem. Chem. Phys.*, 2020, **22**, 1911–1922.

7 H. Ju, M. Kim and J. Kim, *A facile fabrication of n-type Bi2Te3 nanowire/graphene layer-by-layer hybrid structures and their improved thermoelectric performance*, Elsevier, 2015. https://www.sciencedirect.com/science/article/pii/S1385894715005240 (accessed July 18, 2025).

8 C. Han, Q. Sun, Z. Li and S. X. Dou, Thermoelectric Enhancement of Different Kinds of Metal Chalcogenides, *Adv. Energy Mater.*, 2016, **6**(15), 1600498, DOI: 10.1002/aenm.201600498.

9 H. Kageyama, K. Hayashi, K. Maeda, J. P. Attfield, Z. Hiroi, J. M. Rondinelli and K. R. Poeppelmeier, Expanding frontiers in materials chemistry and physics with multiple anions, *Nat. Commun.*, 2018, **9**, 772.

10 X. Shen, K. Pal, P. Acharyya, B. Raveau, P. Boullay, O. I. Lebedev, C. Prestipino, S. Fujii, C.-C. Yang, I.-Y. Tsao, A. Renaud, P. Lemoine, C. Candolfi and E. Guilmeau, Lone Pair Induced 1D Character and Weak Cation–Anion Interactions: Two Ingredients for Low Thermal Conductivity in Mixed-Anion Metal Chalcohalide $CuBiSCl_2$, *J. Am. Chem. Soc.*, 2024, **146**, 29072–29083, DOI: 10.1021/jacs.4c10520.

11 C. Ming, Z. Chen, F. Zhang, S. Gong, X. Wu, J. Jiang, T. Ye, Q. Xu, K. Yang, L. Wang, X. Cao, S. Yang, S. Zhang, Y. Zhang,

J. Shi and Y. Sun, Mixed Chalcogenide-Halides for Stable, Lead-Free and Defect-Tolerant Photovoltaics: Computational Screening and Experimental Validation of $CuBiSCl_2$ with Ideal Band Gap, *Adv. Funct. Mater.*, 2022, **32**(27), 2112682, DOI: 10.1002/adfm.202112682.

12 P. Kush and S. Deka, Multifunctional Copper-Based Quaternary Chalcogenide Semiconductors Toward State-of-the-Art Energy Applications, *ChemNanoMat*, 2019, **5**, 373–402, DOI: 10.1002/cnma.201800321.

13 S. R. Brown, S. M. Kauzlarich, F. Gascoin and G. J. Snyder, $Yb_{14}MnSb_{11}$: New High Efficiency Thermoelectric Material for Power Generation, *Chem. Mater.*, 2006, **18**, 1873–1877, DOI: 10.1021/cm060261t.

14 L.-D. Zhao, S.-H. Lo, Y. Zhang, H. Sun, G. Tan, C. Uher, C. Wolverton, V. P. Dravid and M. G. Kanatzidis, *Ultralow thermal conductivity and high thermoelectric figure of merit in SnSe crystals*, Nature Publishing Group UK London, 2014. https://www.nature.com/articles/nature13184 (accessed July 18, 2025).

15 Y. Dong, B. Eckert, H. Wang, X. Zeng, T. M. Tritt and G. S. Nolas, Synthesis, crystal structure, and transport properties of Cu 2.2 Zn 0.8 SnSe 4- x Te x ($0.1 \leq x \leq 0.4$), *Dalton Trans.*, 2015, **44**, 9014–9019.

16 Y. Dong, H. Wang and G. S. Nolas, Synthesis and thermoelectric properties of Cu excess $Cu_2ZnSnSe_4$, *Phys. Status Solidi RRL*, 2014, **8**, 61–64, DOI: 10.1002/pssr.201308274.

17 X. Y. Shi, F. Q. Huang, M. L. Liu and L. D. Chen, *Thermoelectric properties of tetrahedrally bonded wide-gap stannite compounds Cu2ZnSn1- xInxSe4*, AIP Publishing, 2009. https://pubs.aip.org/aip/apl/article/94/12/122103/151829 (accessed July 18, 2025).

18 C. Wang, Q. Ma, H. Xue, Q. Wang, P. Luo, J. Yang, W. Zhang and J. Luo, Tetrahedral Distortion and Thermoelectric Performance of the Ag-Substituted $CuInTe_2$ Chalcopyrite Compound, *ACS Appl. Energy Mater.*, 2020, **3**, 11015–11023, DOI: 10.1021/acsaem.0c01867.

19 J. Wei, L. Yang, Z. Ma, P. Song, M. Zhang, J. Ma, F. Yang and X. Wang, Review of current high-ZT thermoelectric materials, *J. Mater. Sci.*, 2020, **55**, 12642–12704, DOI: 10.1007/s10853-020-04949-0.

20 M. Guan, K. Zhao, P. Qiu, D. Ren, X. Shi and L. Chen, Enhanced Thermoelectric Performance of Quaternary $Cu_{2-2x}Ag_{2x}Se_{1-x}S_x$ Liquid-like Chalcogenides, *ACS Appl. Mater. Interfaces*, 2019, **11**, 13433–13440, DOI: 10.1021/acsami.9b01643.

21 M. Hong, Z. Chen, L. Yang, Z. Liao, Y. Zou, Y. Chen, S. Matsumura and J. Zou, Achieving $zT > 2$ in p-Type AgSbTe2−xSex Alloys via Exploring the Extra Light Valence Band and Introducing Dense Stacking Faults, *Adv. Energy Mater.*, 2018, **8**(9), 1702333, DOI: 10.1002/aenm.201702333.

22 C. P. Sujith, S. Joseph, T. Mathew and V. Mathew, *Exploring the electronic and optical anisotropy of quasi-one-dimensional ternary chalcogenide CrSbSe3: A DFT study*, Elsevier, 2022. https://www.sciencedirect.com/science/article/pii/S1293255822001212 (accessed July 18, 2025).

23 P. Blaha, K. Schwarz, P. Sorantin and S. B. Trickey, Full-potential, linearized augmented plane wave programs for crystalline systems, *Comput. Phys. Commun.*, 1990, **59**, 399–415, DOI: 10.1016/0010-4655(90)90187-6.

24 K. Schwarz and P. Blaha, Solid state calculations using WIEN2k, *Comput. Mater. Sci.*, 2003, **28**, 259–273, DOI: 10.1016/s0927-0256(03)00112-5.

25 J. P. Perdew, A. Ruzsinszky, G. I. Csonka, O. A. Vydrov, G. E. Scuseria, L. A. Constantin, X. Zhou and K. Burke, Restoring the Density-Gradient Expansion for Exchange in Solids and Surfaces, *Phys. Rev. Lett.*, 2008, **100**, 136406, DOI: 10.1103/PhysRevLett.100.136406.

26 H. J. Monkhorst and J. D. Pack, Special points for Brillouin-zone integrations, *Phys. Rev. B*, 1976, **13**, 5188–5192, DOI: 10.1103/PhysRevB.13.5188.

27 P. Blaha, K. Schwarz, F. Tran, R. Laskowski, G. K. H. Madsen and L. D. Marks, WIEN2k: An APW + lo program for calculating the properties of solids, *J. Chem. Phys.*, 2020, **152**, 074101, DOI: 10.1063/1.5143061.

28 G. K. Madsen, J. Carrete and M. J. Verstraete, BoltzTraP2, a program for interpolating band structures and calculating semi-classical transport coefficients, *Comput. Phys. Commun.*, 2018, **231**, 140–145.

29 A. Kokalj, XCrySDen—a new program for displaying crystalline structures and electron densities, *J. Mol. Graphics Modell.*, 1999, **17**, 176–179, DOI: 10.1016/s1093-3263(99)00028-5.

30 K. Momma and F. Izumi, VESTA 3 for three-dimensional visualization of crystal, volumetric and morphology data, *J. Appl. Cryst.*, 2011, **44**, 1272–1276, DOI: 10.1107/S0021889811038970.

31 C. J. Hawkins, J. A. Newnham, B. Almoussawi, N. L. Gulay, S. L. Goodwin, M. Zanella, T. D. Manning, L. M. Daniels, M. S. Dyer, T. D. Veal, J. B. Claridge and M. J. Rosseinsky, Synthesis, Structure, and Properties of $CuBiSeCl_2$: A Chalcohalide Material with Low Thermal Conductivity, *Chem. Mater.*, 2024, **36**, 4530–4541, DOI: 10.1021/acs.chemmater.4c00188.

32 F. D. Murnaghan, The Compressibility of Media under Extreme Pressures, *Proc. Natl. Acad. Sci. U. S. A.*, 1944, **30**, 244–247, DOI: 10.1073/pnas.30.9.244.

33 P. Wahnón and C. Tablero, Ab initio electronic structure calculations for metallic intermediate band formation in photovoltaic materials, *Phys. Rev. B: Condens. Matter Mater. Phys.*, 2002, **65**, 165115, DOI: 10.1103/PhysRevB.65.165115.

34 M. W. Barsoum, *MAX phases: properties of machinable ternary carbides and nitrides*, John Wiley & Sons, 2013.

35 M. S. Islam, R. Ahmed, M. M. Hossain, M. A. Ali, M. M. Uddin and S. H. Naqib, Ab-initio insights into the physical properties of XIr3 (X= La, Th) superconductors: A comparative analysis, *Results Mater.*, 2024, **22**, 100568.

36 M. S. Dresselhaus, G. Dresselhaus and A. Jorio, *Applications of group theory to the physics of solids*, 2008. https://stuff.mit.edu/afs/athena.mit.edu/course/6/6.734j/OldFiles/www/group-full02.pdf (accessed March 22, 2025).

37 M. I. Naher, M. A. Ali, M. M. Hossain, M. M. Uddin and S. H. Naqib, A comprehensive ab-initio insights into the pressure dependent mechanical, phonon, bonding, electronic, optical,

and thermal properties of CsV3Sb5 Kagome compound, *Results Phys.*, 2023, **51**, 106742.

38 Z. Jin, Y. Wu, S. Li, S. Chen, W. Zhang, Q. Wu and C. Zhang, First-principles calculation of the electronic structure, optical, elastic and thermodynamic properties of cubic perovskite LiBeF3, *Mater. Res. Express*, 2020, **6**, 125116.

39 I. C. Munoz, E. Cruz-Zaragoza, A. Favalli and C. Furetta, *Thermoluminescence property of LiMgF3 erbium activated phosphor*, Elsevier, 2012. https://www.sciencedirect.com/science/article/pii/S096980431200053X (accessed July 28, 2025).

40 A. Ayyaz, N. D. Alkhaldi, S. A. Dar, S. K. Ali, Q. Mahmood, M. S. Al-Buriahi, I. Boukhris and M. M. Al-Anazy, Unveiling theoretical findings on optoelectronic and transport characteristics of Na2ScAu(Cl/Br/I)6 for energy conversion applications, *Opt. Quantum Electron.*, 2025, **57**, 362, DOI: 10.1007/s11082-025-08282-1.

41 Y. U. Peter and M. Cardona, *Fundamentals of semiconductors: physics and materials properties*, Springer Science & Business Media, 2010. https://books.google.com/books?hl=en&lr=&id=5aBuKYBT_hsC&oi=fnd&pg=PR6&dq=10.1007/978-3-642-00710-1&ots=KgCmAkPmwZ&sig=vk5TRi3gbmMZ-kn7epXQMikBcZU (accessed July 28, 2025).

42 G. Murtaza, I. Ahmad, M. Maqbool, H. R. Aliabad and A. Afaq, Structural and optoelectronic properties of cubic CsPbF3 for novel applications, *Chin. Phys. Lett.*, 2011, **28**, 117803.

43 U. V. Ghorpade, M. P. Suryawanshi, M. A. Green, T. Wu, X. Hao and K. M. Ryan, Emerging Chalcohalide Materials for Energy Applications, *Chem. Rev.*, 2023, **123**, 327–378, DOI: 10.1021/acs.chemrev.2c00422.

44 D. Quarta, S. Toso, A. Fieramosca, L. Dominici, R. Caliandro, A. Moliterni, D. M. Tobaldi, G. Saleh, I. Gushchina, R. Brescia, M. Prato, I. Infante, A. Cola, C. Giannini, L. Manna, G. Gigli and C. Giansante, Direct Band Gap Chalcohalide Semiconductors: Quaternary AgBiSCl2 Nanocrystals, *Chem. Mater.*, 2023, **35**, 9900–9906, DOI: 10.1021/acs.chemmater.3c01403.

45 C. D. W. Mosley, M. Failla, D. Prabhakaran and J. Lloyd-Hughes, Terahertz spectroscopy of anisotropic materials using beams with rotatable polarization, *Sci. Rep.*, 2017, **7**, 12337, DOI: 10.1038/s41598-017-12568-0.

46 S. Huang, R.-Z. Li, S.-T. Qi, B. Chen and J. Shen, A theoretical study of the elastic and thermal properties of ScRu compound under pressure, *Phys. Scr.*, 2014, **89**, 065702.

47 C. J. Hawkins, J. A. Newnham, B. Almoussawi, N. L. Gulay, S. L. Goodwin, M. Zanella, T. D. Manning, L. M. Daniels, M. S. Dyer, T. D. Veal, J. B. Claridge and M. J. Rosseinsky, Synthesis, Structure, and Properties of CuBiSeCl2: A Chalcohalide Material with Low Thermal Conductivity, *Chem. Mater.*, 2024, **36**, 4530–4541, DOI: 10.1021/acs.chemmater.4c00188.

48 Z. Zhou, Y. Cui, P.-H. Tan, X. Liu and Z. Wei, Optical and electrical properties of two-dimensional anisotropic materials, *J. Semicond.*, 2019, **40**, 061001, DOI: 10.1088/1674-4926/40/6/061001.

49 M. Thesberg, On the Lorenz number of multiband materials, *Phys. Rev. B*, 2017, **95**, 125206, DOI: 10.1103/PhysRevB.95.125206.

50 E. Haque and M. A. Hossain, Ultra-low lattice thermal conductivity in Cs2BiAgX6 (X = Cl, Br): Potential thermoelectric materials, *arXiv*, preprint, arXiv.1801.03703, 2018, DOI: 10.48550/arXiv.1801.03703.

51 Z. Z. Zhou, H. J. Liu, D. D. Fan, B. Y. Zhao, C. Y. Sheng, G. H. Cao and S. Huang, First-principles study of the thermoelectric properties of quaternary tetradymite BiSbSeTe2, *J. Phys. D: Appl. Phys.*, 2018, **51**, 315501, DOI: 10.1088/1361-6463/aace7b.

52 M. Cutler and N. F. Mott, Observation of Anderson Localization in an Electron Gas, *Phys. Rev.*, 1969, **181**, 1336–1340, DOI: 10.1103/PhysRev.181.1336.

53 J. J. Gong, A. J. Hong, J. Shuai, L. Li, Z. B. Yan, Z. F. Ren and J.-M. Liu, Investigation of the bipolar effect in the thermoelectric material CaMg2Bi2 using a first-principles study, *Phys. Chem. Chem. Phys.*, 2016, **18**, 16566–16574, DOI: 10.1039/C6CP02057G.

54 S. Foster and N. Neophytou, Effectiveness of nanoinclusions for reducing bipolar effects in thermoelectric materials, *arXiv*, preprint, arXiv.1904.05603, 2019, DOI: 10.48550/arXiv.1904.05603.

55 A. Kumar, S. Singh, A. Patel, K. Asokan and D. Kanjilal, Thermoelectric Properties of GaN with Carrier Concentration Modulation: An Experimental and Theoretical Investigation, *Phys. Chem. Chem. Phys.*, 2021, **23**, 1601–1609, DOI: 10.1039/D0CP03950K.

56 S. Goumri-Said, Probing Optoelectronic and Thermoelectric Properties of Lead-Free Perovskite SnTiO3: HSE06 and Boltzmann Transport Calculations, *Crystals*, 2022, **12**, 1317, DOI: 10.3390/cryst12091317.

57 M. Khan and Md. L. Ali, Edge Dislocation and Grain Boundaries Effects on the Mechanical Properties in NiCoAl$N i C o A l$ Medium Entropy Alloy, *Adv. Eng. Mater.*, 2024, **26**, 2400614, DOI: 10.1002/adem.202400614.

58 M. N. M. Nobin, M. L. Ali and M. K. Alam, Edge dislocations, alloy composition, and grain boundaries effects on the mechanical properties in NiCo binary alloy, *Sci. Rep.*, 2024, **14**, 27790.

59 Z. Wu, E. Zhao, H. Xiang, X. Hao, X. Liu and J. Meng, Crystal structures and elastic properties of superhard IrN_2 and IrN_3 from first principles, *Phys. Rev. B: Condens. Matter Mater. Phys.*, 2007, **76**, 054115, DOI: 10.1103/PhysRevB.76.054115.

60 H. Ozisik, K. Colakoglu, H. B. Ozisik and E. Deligoz, Structural, elastic, and lattice dynamical properties of Germanium diiodide (GeI2), *Comput. Mater. Sci.*, 2010, **50**, 349–355, DOI: 10.1016/j.commatsci.2010.08.026.

61 Z. Wu, E. Zhao, H. Xiang, X. Hao, X. Liu and J. Meng, Crystal structures and elastic properties of superhard Ir N 2 and Ir N 3 from first principles, *Phys. Rev. B: Condens. Matter Mater. Phys.*, 2007, **76**, 054115, DOI: 10.1103/PhysRevB.76.054115.

62 R. Hill, The Elastic Behaviour of a Crystalline Aggregate, *Proc. Phys. Soc., London, Sect. A*, 1952, **65**, 349, DOI: 10.1088/0370-1298/65/5/307.

63 D. G. Pettifor, Theoretical predictions of structure and related properties of intermetallics, *Mater. Sci. Technol.*, 1992, **8**, 345–349, DOI: 10.1179/mst.1992.8.4.345.
64 A. Khireddine, A. Bouhemadou, S. Maabed, S. Bin-Omran, R. Khenata and Y. Al-Douri, Elastic, electronic, optical and thermoelectric properties of the novel Zintl-phase Ba2ZnP2, *Solid State Sci.*, 2022, **128**, 106893.
65 W. Bao, D. Liu and Y. Duan, A first-principles prediction of anisotropic elasticity and thermal properties of potential superhard WB3, *Ceram. Int.*, 2018, **44**, 14053–14062.
66 I. R. Shein, Stability, structural, elastic, and electronic properties of polymorphs of the superconducting disilicide YIr2Si2, *Phys. B*, 2011, **406**, 3525–3530.
67 C. Zener, *Elasticity and Anelasticity of Metals*, University of Chicago, 1948.
68 S. F. Pugh, XCII. Relations between the elastic moduli and the plastic properties of polycrystalline pure metals, *Philos. Mag.*, 1954, **45**, 823–843, DOI: 10.1080/14786440808520496.
69 I. N. Frantsevich, F. F. Voronov and S. A. Bakuta, Elastic constants and elastic moduli of metals and nonmetals(In Russian), *Kiev, Izdatel'stvo Naukova Dumka*, 1982, **1982**, 288.
70 L. Kleinman, Deformation Potentials in Silicon. I. Uniaxial Strain, *Phys. Rev.*, 1962, **128**, 2614–2621, DOI: 10.1103/PhysRev.128.2614.
71 Z. Sun, D. Music, R. Ahuja and J. M. Schneider, Theoretical investigation of the bonding and elastic properties of nanolayered ternary nitrides, *Phys. Rev. B: Condens. Matter Mater. Phys.*, 2005, **71**, 193402, DOI: 10.1103/PhysRevB.71.193402.
72 X.-Q. Chen, H. Niu, D. Li and Y. Li, Modeling hardness of polycrystalline materials and bulk metallic glasses, *Intermetallics*, 2011, **19**, 1275–1281.
73 S. I. Ranganathan and M. Ostoja-Starzewski, Universal Elastic Anisotropy Index, *Phys. Rev. Lett.*, 2008, **101**, 055504, DOI: 10.1103/PhysRevLett.101.055504.
74 M. Liao, *hitliaomq/ElasticPOST: ElasticPOST*, 2019, DOI: 10.5281/zenodo.3376758.